Circulation

ORIGINAL RESEARCH ARTICLE

Targeting uPARAP Modifies Lymphatic Vessel Architecture and Attenuates Lymphedema

Fabrice Gucciardo, PhD*; Alizée Lebeau, PhD*; Sébastien Pirson, PhD*; Florence Buntinx, MSc*; Elitsa Ivanova, PhD*; Silvia Blacher, PhD; Pascal Brouillard, PhD; Jonathan Deroye, MSc; Louis Baudin, MSc; Alexandra Pirnay, MSc; Florent Morfoisse, PhD; Claire Villette, PhD; Christophe Nizet, MD; François Lallemand, MD, PhD; Carine Munaut, PhD; Kari Alitalo, MD, PhD; Liesbet Geris, PhD; Miikka Vikkula, MD, PhD; Marine Gautier-Isola, PhD†; Agnès Noel, PhD†

BACKGROUND: Lymphedema is an incurable disease associated with lymphatic dysfunction that causes tissue swelling and fibrosis. We investigated whether lymphedema could be attenuated by interfering with uPARAP (urokinase plasminogen activator receptor-associated protein; *Mrc2* gene), an endocytic receptor involved in fibrosis and lymphangiogenesis.

METHODS: We generated mice with lymphatic endothelial cell (LEC)–specific *uparap* deficiency and compared them with constitutive knockout mice by applying a preclinical model of secondary lymphedema (SL). Computerized methods were applied for 2-dimensional and 3-dimensional image quantifications. Cellular effects of uPARAP deletion on lymphatic permeability were assessed by small interfering RNA–mediated silencing in human dermal LECs and a pharmacologic treatment targeting ROCK (Rho-associated coiled coil containing kinase), an established regulator of cell junctions. The uPARAP and vascular endothelial cadherin partnership was investigated through proximity ligation assay, coimmunoprecipitation, and immunostaining. An in silico model was generated to analyze the fluid-absorbing function of the lymphatic vasculature. To interfere with uPARAP, its downregulation was achieved in vivo through a gapmer approach.

RESULTS: *uparap* deficiency mitigated several key pathologic features of SL, including hindlimb swelling, epidermal thickening, and the accumulation and size of adipocytes. In both global and LEC-conditional *uparap*-deficient mice, induction of SL led to a distinctive labyrinthine vasculature, defined herein by twisted and hyperbranched vessels with overlapping cells. This topology, mainly composed of pre–collecting vessels, correlated with reduced SL, but not with change in fibrosis, highlighting the importance of uPARAP in regulating LEC functions in a lymphedematous context. In vitro, uPARAP knockdown in LECs impaired vascular endothelial growth factor C–mediated endosomal trafficking of vascular endothelial cadherin and induced overlapping cell junctions. The pharmacologic inhibition of ROCK recapitulated cell superimposition in vitro and the labyrinthine vasculature in vivo with attenuated SL. Computational modeling of labyrinthine lymphatic vasculature supported the observation on their improved fluid-absorbing function in comparison with a normal hierarchic network. These data provide proof of concept of inducing a labyrinthine topology to treat SL. For therapeutic purposes, we validated the use of an anti-uPARAP gapmer to induce a labyrinthine vasculature and attenuate SL formation.

CONCLUSIONS: Our findings provide evidence that downregulating uPARAP expression can induce a beneficial remodeling of lymphatic vasculature that attenuates lymphedema through a cell junction–based mechanism, offering a novel therapeutic pathway for lymphedema.

Key Words: adherens junctions ■ cadherins ■ lymphatic vessels ■ lymphedema

Correspondence to: Agnès Noel, PhD, Laboratory of Tumor and Development Biology, Tour de Pathologie, B23, Avenue Hippocrate 13, 4000 Liège, Belgium. Email agnes.noel@uliege.be
*F. Gucciardo, A. Lebeau, S. Pirson, F. Buntinx, and E. Ivanova contributed equally.
†M. Gautier-Isola and A. Noel contributed equally.
Supplemental Material is available at https://www.ahajournals.org/doi/suppl/10.1161/CIRCULATIONAHA.124.072093.
For Sources of Funding and Disclosures, see page 1428.

Circulation is available at www.ahajournals.org/journal/circ

Clinical Perspective

What Is New?

- Global and lymphatic endothelial cell–specific deletion of *uparap* (urokinase plasminogen activator receptor-associated protein) in mice leads to attenuated secondary lymphedema.
- The formation of a labyrinthine lymphatic vasculature characterized by hyperbranched and twisted vessels is associated with attenuated lymphedema.
- uPARAP governs vascular endothelial growth factor C–driven vascular endothelial cadherin endosomal trafficking in human lymphatic endothelial cells independently of its role in collagen remodeling.

What Are the Clinical Implications?

- uPARAP is a new target to treat lymphedema.
- Inducing the formation of a labyrinthine vasculature reduces lymphedema formation.
- Targeting uPARAP with antisense oligonucleotides has therapeutic potential to treat lymphedema.

Nonstandard Abbreviations and Acronyms

3D	3-dimensional
AAV	adeno-associated viruses
GTPase	guanosine triphosphatase
IgG	immunoglobulin G
ITGA9	integrin α-9
JAIL	junction-associated intermittent lamellipodia
JNK	c-Jun N-terminal kinase
KD-LEC	knockdown lymphatic endothelial cells
LEC	lymphatic endothelial cell
Rac1	Ras-related C3-rich protein 1
RhoA	Ras homolog family member A
ROCK	rho-associated coiled coil containing kinase
siRNA	small interfering RNA
SL	secondary lymphedema
uPARAP	urokinase plasminogen activator receptor-associated protein
VE-cadherin	vascular endothelial cadherin
VEGF-C	vascular endothelial growth factor–C
VEGFR	vascular endothelial growth factor receptor
WT	wild-type

Lymphedema, an incurable disorder of the lymphatic vascular system, is a chronic and debilitating condition characterized by impaired lymphatic drainage, tissue swelling, and fibrosis.[1] Lymphedema can manifest either as primary lymphedema, mostly attributable to genetic causes, or secondary lymphedema (SL), resulting from cancer treatment or lymphadenectomy.[2] The vascular endothelial growth factor C (VEGF-C)/vascular endothelial growth factor receptor 3 (VEGFR-3) signaling pathway is a major driver of embryonic, postnatal, and pathologic lymphatic vascular network development.[3–5] Sequence variations in genes associated with this pathway, including *VEGF-C*, *FLT4*, *CCBE1*, and *ADAMTS3*, have been detected in patients with primary lymphedema.[2,6] Lymphedema treatments encompass manual massage, limb compression therapies, and surgical interventions.[1] Preclinical attempts to treat lymphedema in mice have used pro-lymphangiogenic factors, such as VEGF-C[7] and various biomaterials with and without stem cells, and inhibitors of fibrosis factors (anti– transforming growth factor–β)[8] or tissue inflammation.[9,10] A phase 2 clinical trial has indicated safety and potential benefit of adenoviral VEGF-C and lymph node transfer in lymphedema.[11] Whether a modulation of other features of lymphatic vessels or surrounding fibrotic tissues is required for lymphedema treatment remains to be explored.

We explored the function of uPARAP (urokinase plasminogen activator receptor-associated protein)/Endo180 (*Mrc2*) in an SL model in mice. uPARAP, primarily a collagen receptor involved in both fibrotic and lymphangiogenic processes, contributes to collagen turnover and directional cell migration.[12–14] Although uPARAP is expressed mostly by mesenchymal and endothelial cells,[15] its role in vascular biology remains poorly understood.[16] We previously demonstrated that uPARAP restricts VEGFR-2/VEGFR-3 heterodimerization, enhances VEGFR-3/JNK (c-Jun N-terminal kinase)/Rac1 (Ras-related C3-rich protein 1) signaling, impairs directional lymphatic endothelial cell (LEC) migration, and increases lymphangiogenesis.[16]

We generated LEC-specific *uparap*-deficient mice. We used them, as well as global *uparap*-deficient mice, as experimental models to interfere with collagen or lymphatic remodeling, or both, during SL formation. To mimic the generation of SL in patients with cancer, we subjected 1 hindlimb to irradiation followed by lymph node resection and lymphatic vessel ligation in mice. Both constitutive and LEC-specific *uparap*-deficient mice exhibited an SL phenotype consisting of a cutaneous lymphatic network of hyperbranched and twisted vessels, along with overlapping cell junctions, collectively termed labyrinthine vasculature. This vascular pattern correlated with attenuated SL formation versus wild-type (WT) control mice. Our findings demonstrate an unprecedented role of uPARAP in lymphedema and underscore the therapeutic potential of labyrinthine vasculature induction, uPARAP downregulation, or both.

ORIGINAL RESEARCH ARTICLE

METHODS

Data Availability Statement

Source data for figures and supplemental figures are available from the corresponding author on reasonable request. Materials used to conduct the research are included in the article or in the Methods in the Supplemental Material.

Animals and Study Design

All animal experiments were approved by the institutional animal care and use committee at the University of Liege (approval 20-2204). Female mice, 6 to 8 weeks of age, were housed in a standard environment with controlled light and temperature within ventilated cages (4 or 5 mice per cage), with food and water ad libitum. Power calculations were performed to calculate sample size. Animals were randomly assigned to either treatment or control groups. All histologic examinations were performed in a blind fashion.

Secondary Hindlimb Lymphedema Model

The lymphedema model combined hindlimb irradiation and surgery, as described.[17] Bilateral limb volume was measured every 3 days using a caliper. To reduce individual variability, limb volume was normalized for each animal by calculating the percentage change from the control limb (nonoperated right limb). In some assays, mice were injected with recombinant adeno-associated viruses (AAVs) encoding either domains 1 through 3 of VEGFR-3 (AAV-VEGFR-3[1-3]-IgG-Fc; VEGF-C trap)[18] or domains 4 through 7 of VEGFR-3 (AAV-VEGFR-3[4-7]-IgG-Fc),[19] both fused to the immunoglobulin (IgG) Fc domain (Supplemental Material).

Three-Dimensional Reconstruction of Lymphatic Vessels

Three-dimensional (3D) lymphatic network reconstruction was conducted on whole skin samples. After immunohistochemical staining, images were captured using a Leica SP5/SP8a confocal microscope, and processed and analyzed with MATLAB 2022b. Vasculature complexity was assessed by measuring branching density (branching per total network length) and tortuosity (actual path length divided by the linear distance),[20] and assigned a score ranging from 1, indicating a straight line, to higher values, indicating more complex, twisted vessel shapes.

In Vitro Assays

Primary human LECs (HMVEC-dLy; Lonza) were cultured in EGM2-MV medium (complete medium; Lonza) until 80% confluence. LECs were transfected with a pool of small interfering RNAs (siRNAs) targeting uPARAP or control siRNAs. Cells were stimulated with recombinant human VEGF-C (400 ng/mL; Abcam), human VEGF-$C_{Cys156Ser}$ (500 ng/mL), or human VEGF-A (400 ng/mL; both from R&D Systems). Proximity Ligation Assay[16,21] and Pulse-Chase Assay[22,23] were performed as described. Vascular endothelial (VE) cadherin internalization and recycling analyses were adapted from previous studies.[24,25]

Computational Modeling

Fluid velocity (V) through the vessel wall was modeled as a function of tissue fluid pressure (p) and represented by $V=L_p p$, where L_p is the seepage coefficient. This model is grounded in poroelasticity theory.[26,27] Poroelastic finite-element methods are widely used to estimate pore pressure and fluid flow within the microporosity of biologic tissues such as bone[28–30] and dermis.[31–33] For the dermis, we assigned $Lp=30\ \mu m^2 \cdot s \cdot kg^{-1}$,[34] Young modulus $E=200$ kPa,[25] Poisson ratio $\nu=0.47$,[25] permeability $K=1\times10^{-14}\ m^4 \cdot N^{-1} \cdot s^{-1}$,[31,35] void ratio $\varphi=0.05$,[28,30] and specific weight of wetting liquid $w=9.807\ kN/m^3$.

Statistics

Statistical analyses were performed using GraphPad Prism 9 (GraphPad Software) or MATLAB R2021a (MathWorks, Inc.). Data normality was evaluated using the Shapiro-Wilk test and visually confirmed with QQ plot. Based on data distribution, as well as the number of groups and measures analyzed, we selected appropriate parametric or nonparametric tests, as specified in the figure legends. For normally distributed data, statistical tests included 1-way or 2-way (repeated-measures or not repeated-measures) ANOVA, followed by multiple comparisons using Holm-Šídák correction, unpaired or ratio paired *t* tests, or 1-sample *t* tests. Data are presented as mean±SEM. For non-normally distributed data, analyses included Kruskal-Wallis test followed by Dunn test with Bonferroni correction, Kolmogorov-Smirnov test, or Mann-Whitney *U* test. These data are reported as medians with interquartile ranges. Statistical significance was determined at $P<0.05$, denoted as follows: $^*P<0.05$, $^{**}P<0.01$, $^{***}P<0.001$, $^{****}P<0.0001$.

Additional details of experimental procedures are provided in the Supplemental Material.

RESULTS

Constitutive *uparap*$^{-/-}$ Mice Exhibit a Labyrinthine Lymphatic Vasculature Associated With Attenuated SL

To induce SL in the hindlimb of *uparap*$^{+/+}$ and global *uparap*$^{-/-}$ mice, we combined local irradiation followed by lymph node resection and lymphatic vessel ligation of one limb, and the other limb was used as control (Figure 1A). SL progression was monitored by measuring bilateral limb thickness, which revealed a 200% to 250% increase in limb volume in *uparap*$^{+/+}$ versus control mice (Figure 1B). *uparap*$^{-/-}$ mice exhibited a 31% reduction of limb volume change versus *uparap*$^{+/+}$ mice. Histologically assessed key lymphedema features revealed epidermal/dermal thickening, increased inflammation (F4/80$^+$ macrophage infiltration), and fibroadipose tissue accumulation (Figure S1). In *uparap*$^{-/-}$ mice, SL skins exhibited reduced epidermal thickening, as well as decreased accumulation of adipocytes exhibiting a smaller size (Figure S1B and S1E through S1G; $P<0.005$). The 2 genotypes exhibited comparable inflammation and fibrosis, as indicated by macrophage infiltration (Figure S1D) and the

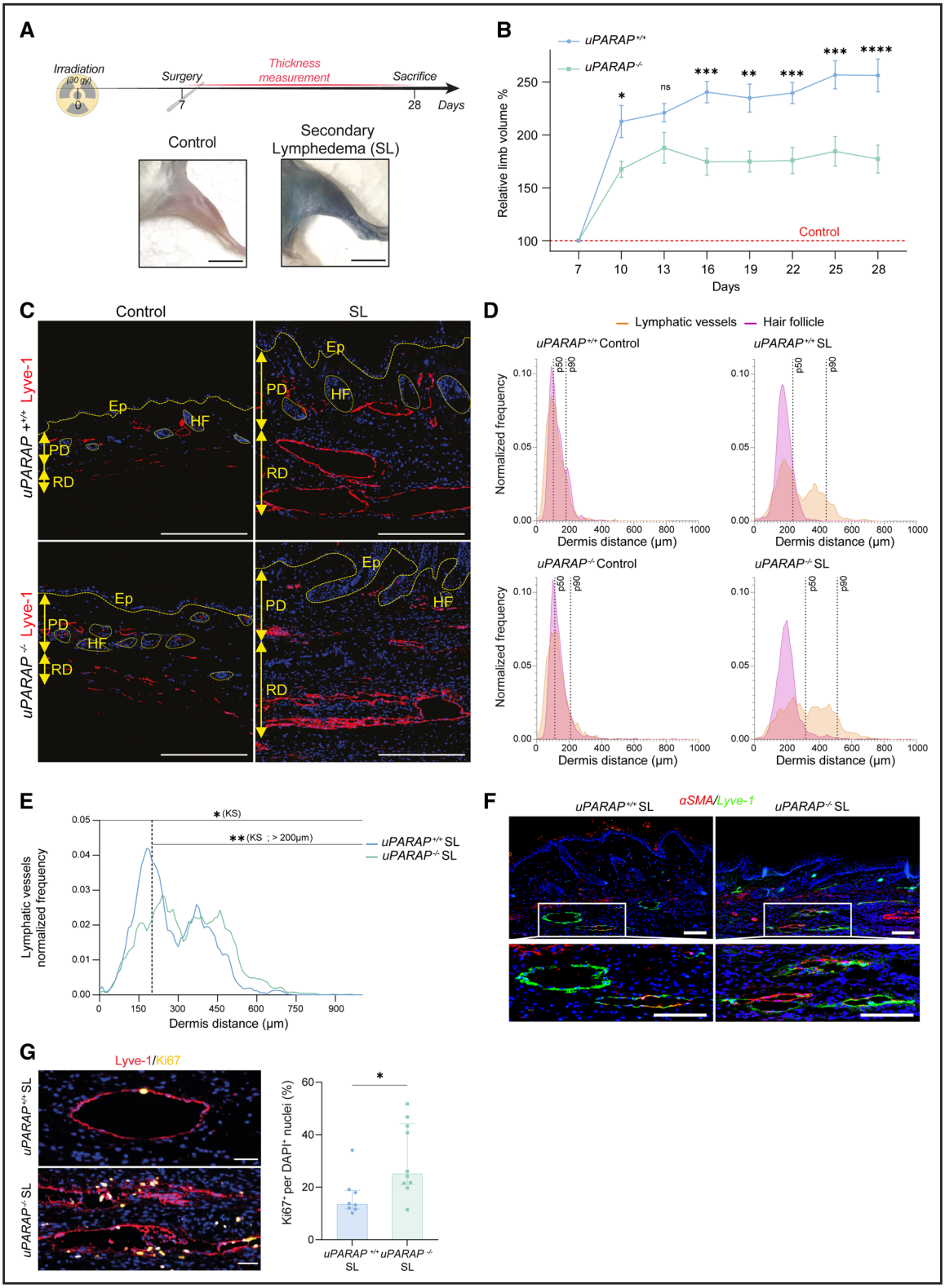

Figure 1. *uparap* deficiency attenuates secondary lymphedema.
Secondary lymphedema (SL) was induced in WT ("*uPARAP*$^{+/+}$") (n=8) and *uparap*-deficient ("*uPARAP*$^{-/-}$") (n=10) mice. **A**, Timeline of the experiment with representative images of control and SL limb at day 28. Scale bars=1 cm. **B**, Follow-up of the relative volume of hindlimb subjected to SL induction in *uPARAP*$^{+/+}$ or *uPARAP*$^{-/-}$ mice. Results are expressed as percentage of control limb volume (100%, dotted line). Data are mean±SEM. **C**, Representative images of Lyve-1^{+} vessels (red) with nuclei (blue) in control and SL skin. Scale bars=250 µm. **D**, Spatial distribution of lymphatic vessels (orange) as the distance from the basal epithelial layer (distance=0 on the *x* axis). Hair follicle density (purple) is presented to delineate hair follicle–associated lymphatic vessels in the papillary dermis. P50 and P90 percentiles correspond to the (*Continued*)

Figure 1 Continued. distance at which 50% and 90% of lymphatic vessels are localized, respectively. **E**, Spatial distribution of lymphatic vessels in SL skins of *uPARAP*$^{+/+}$ (blue) and *uPARAP*$^{-/-}$ (green) mice were superimposed. The dashed line at 200 µm delineates approximatively the papillary and the reticular dermis. **F**, Representative images (with higher magnification of the area delineated with a white rectangle) of Lyve-1^{+} (green) and α–smooth muscle actin (αSMA)$^{+}$ (red) vessels with nuclei (blue) in *uPARAP*$^{+/+}$ and *uPARAP*$^{-/-}$ SL skins. Scale bars=100 µm. **G**, Representative images (left) of Ki67^{+} cells (yellow) associated with deeper Lyve-1^{+} vessels (red) of SL skins. The graph (right) corresponds to the quantification of Ki67^{+} cells per vessel–associated DAPI^{+} nuclei (blue). Data are medians with interquartile ranges. Scale bars=50 µm. Statistical tests used were 2-way repeated-measures ANOVA with Holm-Sidak post hoc test for multiple comparisons (**B**), Kolmogorov-Smirnov test to compare 2 distribution curves (for the total curve or for distances >200 µm; **E**), and Mann-Whitney *U* test (**G**). **P*<0.05; ***P*<0.01; ****P*<0.001; *****P*<0.0001. Ep indicates epidermis; HF, hair follicles; PD, papillary dermis; and RD, reticular dermis.

scar index, which distinguishes thick and thin collagen fibers (Sirius red staining; Figure S1H and S1I). Therefore, SL severity was significantly reduced in *uparap*$^{-/-}$ mice without affecting fibrosis.

In normal skins of both *uparap*$^{+/+}$ and *uparap*$^{-/-}$ mice, lymphatic vessels identified through Lyve-1 staining were found underneath the epidermis and closely associated with hair follicles within the papillary dermis (Figure 1C).[36] Spatial distribution of lymphatic vessels was determined by calculating the vessel frequency as a function of the distance from the basal epithelial layer (Figure 1D). The distance at which up to 90% of Lyve-1^{+} vessels were detected (90th percentile), was similar in *uparap*$^{+/+}$ (181.55 µm) and *uparap*$^{-/-}$ (208.79 µm) mice (Figure 1D, left).

In SL skins, 2 distinct types of cutaneous vessels were identified: narrow lymphatic vessels associated with hair follicles in the papillary dermis, similar to those in normal skins, accounting for approximately half of the vessels (50th percentile), and large lymphatic vessels deeply located in the reticular dermis at a distance >200 µm from the epidermis (Figure 1C and 1D, right). A comparison of lymphatic vessel distribution curves in the SL condition indicated a significant difference between the 2 genotypes (*P*=0.0138), particularly in the reticular dermis (*P*=0.0036 for region >200 µm; Kolmogorov-Smirnov tests; Figure 1E). In *uparap*$^{+/+}$ SL mice, 55% of lymphatic vessels were detected at a distance <200 µm, whereas in *uparap*$^{-/-}$ SL mice, 38% of vessels were detected in papillary and 62% in reticular dermis (>200 µm; Figure 1D and 1E).

The main morphologic differences in SL lymphatic vasculature were observed in the reticular dermis, where lymphatic vessels of both genotypes exhibited α–smooth muscle actin and Lyve-1 staining, indicating precollecting vessel characteristics (Figure 1F). In situ hybridization and immunohistochemistry revealed uparap expression in those Lyve-1^{+}/*Prox1*$^{+}$/αSMA^{+} precollecting vessels (Figure S2A). In *uparap*$^{-/-}$ SL skins, lymphatic sections appeared more juxtaposed (Figure 1C, 1F, and 1G), with their LECs exhibiting a higher proliferation ratio assessed by Ki-67 index (*P*<0.05; Figure 1G). Computerized 3D confocal image analysis of lymphatic vasculature in the reticular dermis (Figure 2A) showed increased branching density and vessel tortuosity, indicating twisting of these vessels in *uparap*$^{-/-}$ SL skins (Figure 2B). Valves were detected in those vessels as assessed by ITGA9 (integrin α-9) staining, and their number was similar in both genotypes (Figure S2B and S2C).

VE-cadherin staining revealed atypical LEC–LEC junctions with overlapping cells in *uparap*$^{-/-}$ SL skins (Figure 2C). This disorganized vessel structure was also associated with uPARAP deficiency in mouse ears treated with VEGF-C to induce lymphangiogenesis (Figure 2D). These overlapping cytoplasmic extensions were positive for Lyve-1 (Figure S2D), further supporting their precollecting vessel feature. However, we cannot exclude the presence of valves close to some atypical junctions. We called this distinct lymphatic vascular pattern in *uparap*$^{-/-}$ mice, marked by highly branched and twisted precollecting vessels, labyrinthine vasculature.

LEC-Specific *uparap* Ablation Phenocopies the Labyrinthine Vasculature and Attenuates SL

To specifically delete *Mrc2* gene encoding uPARAP in LECs, we generated *uparap* floxed mice (*uPARAP*$^{fl/fl}$) and crossed them with *Prox1CreER*^{T2} mice, which express tamoxifen-inducible Cre recombinase in *Prox1*$^{+}$ LECs (Figure 3A). This new *uPARAP*$^{\Delta LEC}$ mouse model was generated in a C57BL6 background, whereas constitutive *uparap*$^{-/-}$ mice were in a FvBN background. We confirmed similar SL attenuation across backgrounds, indicating that the phenotype was independent of the genetic background (data not shown). LEC-specific deletion of *uparap* was verified by reverse transcription quantitative polymerase chain reaction on fluorescence-activated cell sorted skin cells (Figure 3B; Figure S3 [for population purity]). *uPARAP*$^{\Delta LEC}$ mice exhibited SL attenuation comparable to global *uparap*$^{-/-}$ mice (reductions in limb volume of 42% and 31%, respectively; Figure 1B; Figure 3C). The atypical lymphatic vasculature features were recapitulated in *uPARAP*$^{\Delta LEC}$ mice (Figure 3D through 3F), including increased LEC proliferation index (Figure 3D), vessel tortuosity, and hyperbranching (Figure 3E and 3F) in SL skins. These findings confirmed that the observed phenotype is specifically attributable to *uparap* deficiency in LECs.

uPARAP Silencing Alters VE-Cadherin–Mediated Cell Junctions in Human Primary LECs

To silence uPARAP expression, human primary LECs were transfected in vitro with multiple uPARAP siRNAs (knockdown LECs [KD-LECs]; Figure S4). At the steady state, both control LECs and KD-LECs organized into a

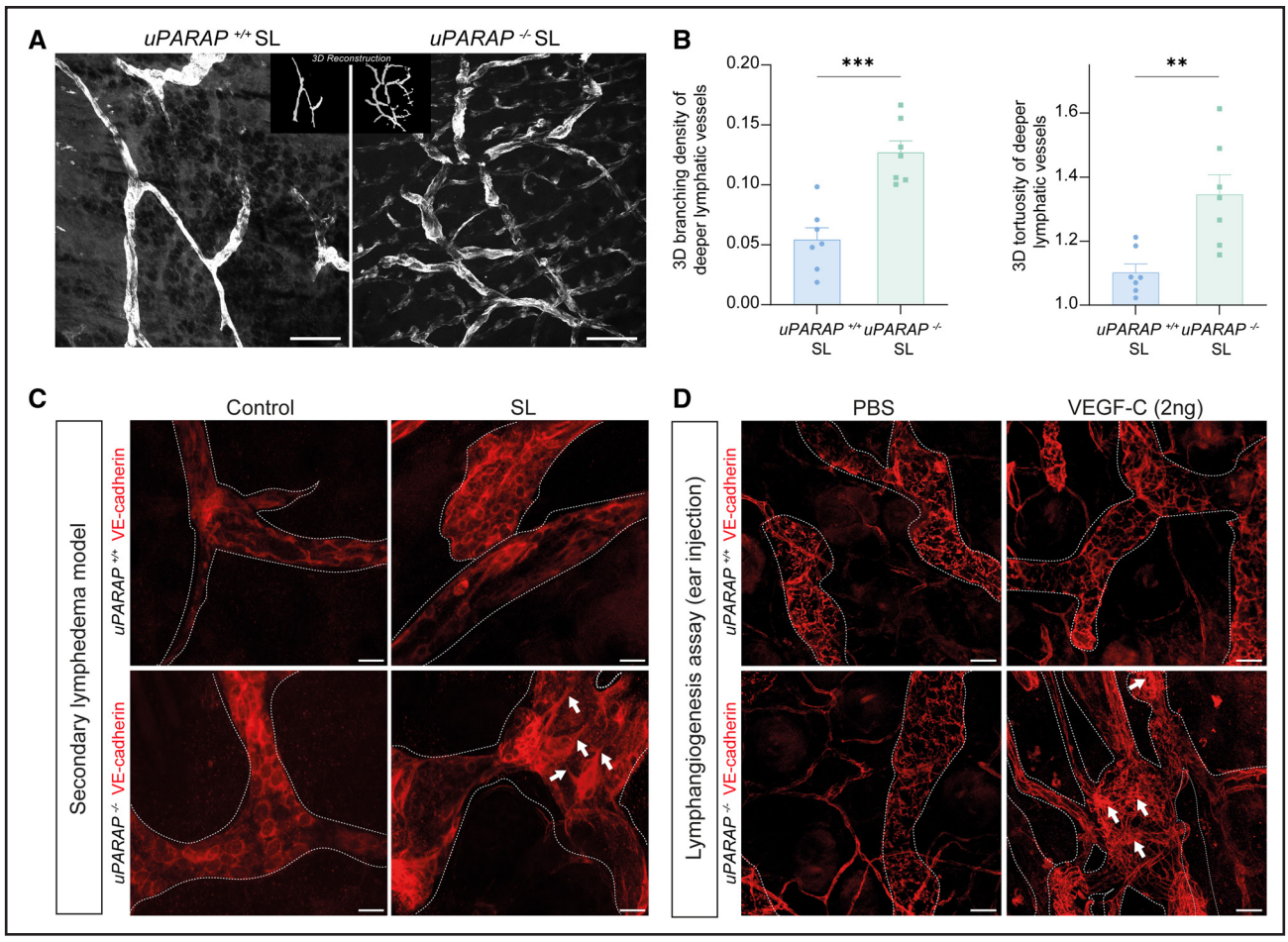

Figure 2. *uparap* deficiency is associated with a more complex and ramified labyrinthine lymphatic vasculature with overlapping cells.

A, Z-stack projections of deeper Lyve-1$^+$ lymphatic vessels in secondary lymphedema (SL) skin. Binarized 3-dimensional (3D) reconstructed images used for quantification are shown in the top corners. Scale bars=250 µm. **B**, Three-dimensional quantification of deeper Lyve-1$^+$ vessels in whole-mount SL skin samples of WT ("*uPARAP*$^{+/+}$") and *uparap*-deficient ("*uPARAP*$^{-/-}$") mice. The 2 graphs correspond to 3D branching density (left) and 3D tortuosity (right). Data are mean±SEM. Statistical test: unpaired *t* test. $^{**}P<0.01$; $^{***}P<0.001$. **C** and **D**, Representative Z-stack projections of vascular endothelial (VE) cadherin staining (red) in Lyve-1$^+$ vessels delineated by dashed lines in *uPARAP*$^{+/+}$ and *uPARAP*$^{-/-}$ mice subjected to SL (**C**) or vascular endothelial growth factor–C (VEGF-C) injection (2 ng) into the ear (**D**). Arrows show overlapping cytoplasmic extensions. Scale bars=50 µm.

cobblestone cell monolayer. However, VEGF-C stimulation for 24 hours induced the elongation and alignment of control LECs (Figure 4A). In contrast, VEGF-C–stimulated KD-LECs started to overlap, showing disruption in VE-cadherin-based cell–cell junctions, characterized by overlapping cytoplasmic extensions, mirroring the in vivo findings (Figure 4A; Figure 2E and 2F). This distinctive cell behavior was validated by live-cell imaging microscopy (Videos S1 and S2). We confirmed that the phenotype observed was solely VEGF-C–dependent, because no cellular overlapping could be observed in KD-LECs treated with VEGF-A (ligand of VEGFR-2 homodimer) or VEGF-$C_{Cys156Ser}$ (ligand of VEGFR-3/VEGFR-3 homodimer) stimulation (Figure S5A). These data are in line with a previous study reporting that VEGF-C triggers the VEGFR-2/VEGFR-3 signaling pathway in KD-LECs.[16]

The observed types of LEC–LEC junctions were classified into 7 categories based on their morphology in high magnification under confocal microscopy: linear, reticular, finger, spike, zipper, wave-like, and overlapping protrusions (Figure 4C and 4D).[23] The so-called wave-like junction, characterized by VE-cadherin spots without gaps (Figure 4C), may fit into the junction-associated intermittent lamellipodia (JAIL) definition, a mechanism whereby endothelial cells remodel junctions and renew cell–cell contacts by transiently decreasing membrane-bound VE-cadherin.[37] When LECs were starved, uPARAP silencing increased the percentage of overlapping protrusions (10.6% in KD-LECs versus 1.5% in control LECs) and wave-like lamellipodia (15.4% in KD-LECs versus 10.4% in control LECs; $P<0.05$; Figure 4C). These atypical junctions were prominent when uPARAP silencing was combined with VEGF-C stimulation. Indeed,

ORIGINAL RESEARCH ARTICLE

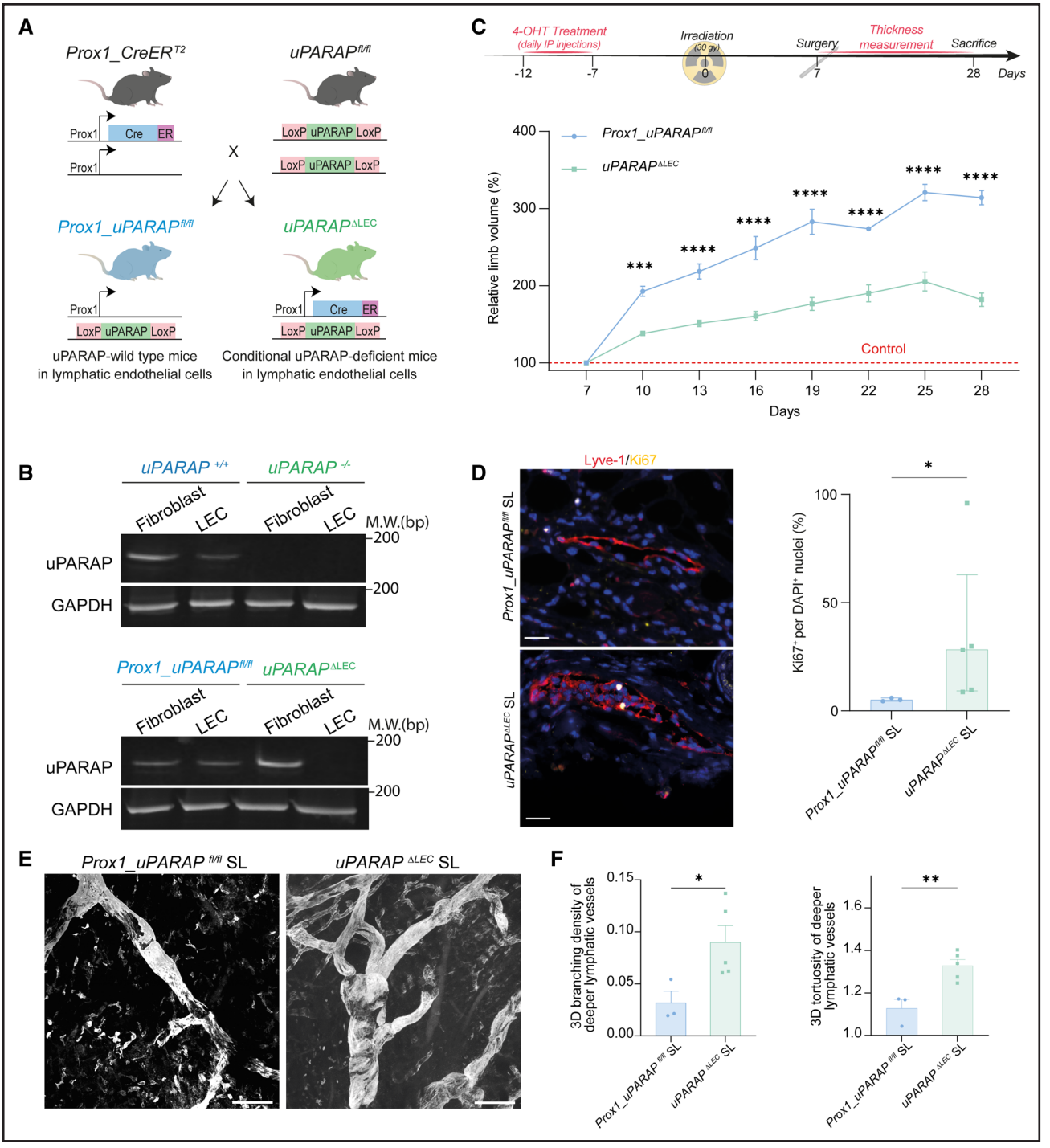

Figure 3. Conditional deletion of *uparap* in lymphatic endothelial cells phenocopies global *uparap* deficiency and results in secondary lymphedema attenuation.

A, To delete *uparap* (*uPARAP*$^{\Delta LEC}$ mice), specifically in lymphatic endothelial cells (LECs), we generated *uparap* floxed mice (*uPARAP*$^{fl/fl}$) and crossed them with *Prox1CreER*^{T2} deletor mice expressing a tamoxifen-inducible Cre recombinase in *Prox1*$^{+}$ LECs. **B**, Reverse transcription quantitative polymerase chain reaction analysis of uparap and Gapdh mRNA in LECs (CD31^{+}, PDPN^{+}) and fibroblasts (CD31^{-}, PDPN^{+}) sorted by fluorescence-activated cell sorting from *uPARAP*$^{+/+}$, *uPARAP*$^{-/-}$, *Prox1_uPARAP*$^{fl/fl}$, and *uPARAP*$^{\Delta LEC}$ skins. **C**, Timeline (above) of the 4-OHT treatment and secondary lymphedema (SL) induction in uPARAP-wild-type mice (*Prox1_uPARAP*$^{fl/fl}$ mice; n=3) and conditional *uPARAP*$^{-/-}$ mice in LECs (*uPARAP*$^{\Delta LEC}$; n=7). Follow-up (below) of the relative volume of hindlimb subjected to SL induction. Results are expressed as percentage of control limb volume (100%, dotted line). Data are mean±SEM. **D**, Representative images (left) and quantification (right) of Ki67^{+} (yellow) per DAPI^{+} (blue) nuclei in deeper Lyve-1^{+} vessels (red) in *Prox1_uPARAP*$^{fl/fl}$ and *uPARAP*$^{\Delta LEC}$ SL skins. Scale bar=20 µm. Data are medians and interquartile ranges. **E**, Z-stack projections of deeper Lyve-1^{+} lymphatic vessels in SL skin. Scale bars=250 µm. **F**, Three-dimensional quantification of deeper Lyve-1^{+} vessels in whole-mount SL skin samples: 3-dimensional (3D) branching density (left) and 3D tortuosity (right). Data are mean±SEM. Statistical tests: 2-way repeated-measures ANOVA with Holm-Sidak post hoc test for multiple comparisons (**C**), Mann-Whitney *U* test (**D**), and unpaired *t* test (**F**). **P*<0.05; ***P*<0.01; ****P*<0.001; *****P*<0.0001).

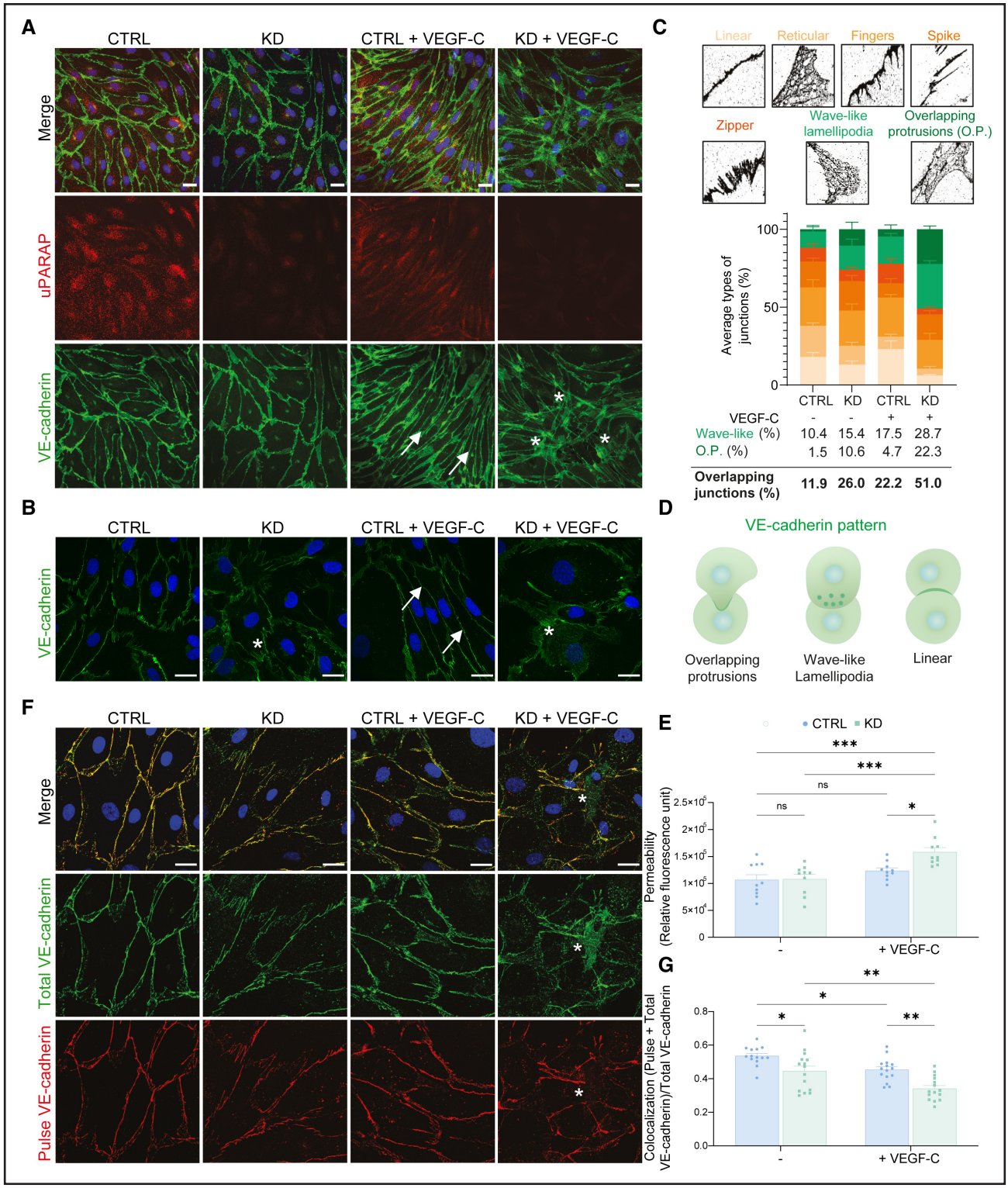

Figure 4. uPARAP silencing enhances overlapping conformation of cell–cell junctions in lymphatic endothelial cells after vascular endothelial growth factor–C treatment.

Lymphatic endothelial cells (LECs) were transfected with a pool of 4 small interfering RNAs against uPARAP (knockdown [KD]) or a pool of 4 control small interfering RNAs. **A** through **C**, Vascular endothelial (VE) cadherin and uPARAP (urokinase plasminogen activator receptor-associated protein) immunolabeling of transfected cells treated or not with vascular endothelial growth factor–C (VEGF-C) for 24 hours (**A**) or 2 hours (**B** and **C**). Arrows show linear junctions and asterisks indicate overlapping junctions (referring to wave-like lamellipodia or wave-like and overlapping protrusions [OP]). Quantification of 7 different cell–cell junctions (as depicted in annotated images; **B**) determined in 5 independent microscope fields by condition and by experiment (**C**). Data are mean±SEM from 3 independent experiments (**C**). **D**, Schematic representation of 3 main cell–cell junction types modulated by uPARAP silencing. **E**, Relative permeability of FITC-dextran (40 kDa) assessed after (*Continued*)

Figure 4 Continued. 60 minutes in KD compared with wild-type LECs, stimulated or not with VEGF-C. Data are mean±SEM from 10 independent experiments. **F**, Pulse-chase assay. Extracellular VE-cadherin (pulse VE-cadherin; red) was labeled at 4 °C on live cells. Two hours after VEGF-C stimulation, cells were fixed and total VE-cadherin (green) was labeled with permeabilizing conditions. **G**, Graph corresponds to quantification of 5 independent microscope fields by condition and by experiment. Data are mean±SEM from 3 independent experiments. Asterisks indicate overlapping junctions. Scale bars=20 µm. Statistical test: 2-way ANOVA with Holm-Sidak post hoc test for multiple comparisons (**E** and **G**). *$P<0.05$; **$P<0.01$; ***$P<0.001$.

>50% of the junctions were either overlapping protrusions (22.3% in KD-LECs versus 4.7% in control LECs) or wave-like lamellipodia (28.7% in KD-LECs versus 17.5% in control LECs; $P<0.05$; Figure 4C and 4D). Furthermore, the shift in cell–cell junction morphologies was correlated with an increased permeability as assessed in Boyden chamber assays ($P<0.05$; Figure 4E).

uPARAP Silencing Impairs VE-Cadherin Recycling

To investigate how uPARAP regulates LEC–LEC junctions, we next assessed total VE-cadherin level and its phosphorylation status (pY658 and pY685). However, neither total VE-cadherin level nor its phosphorylation status were modulated by uPARAP silencing, either in steady state or upon VEGF-C stimulation (Figure S5B).

To investigate the fate of VE-cadherin after internalization, we took advantage of an antibody targeting VE-cadherin extracellular domain to label cell-surface VE-cadherin at 4 °C (pulsed VE-cadherin) and monitored it after VEGF-C stimulation at 37 °C. In control LECs, both pulsed and total VE-cadherin were predominantly present at the cell surface, indicating smooth intracellular recycling (Figure 4F and 4G). However, we found a significant reduction in pulsed VE-cadherin concentration at the cell membrane with barely distinguishable cellular junctions in KD-LECs, which was exacerbated after VEGF-C stimulation (Figure 4F and 4G; $P<0.05$). The pulsed and total VE-cadherin to total VE-cadherin ratio (yellow to green positive pixels) was highly reduced in KD-LECs after VEGF-C treatment (Figure 4F and 4G; $P<0.05$). Live imaging of cell-surface VE-cadherin confirmed a defect in LEC–LEC junction establishment along with an accumulation of intracellular VE-cadherin (Videos S1 and S2). Together, these data indicate a defect in VE-cadherin recycling to the cell surface in absence of uPARAP that is exacerbated by VEGF-C.

uPARAP Governs VE-Cadherin Endosomal Trafficking

To ascertain the interplay between VE-cadherin and uPARAP, we conducted a coimmunoprecipitation assay using anti-uPARAP antibodies. VE-cadherin/uPARAP complexes were detected after 10 minutes of VEGF-C stimulation, but not at later time points, suggesting a transient, VEGF-C–dependent interaction (Figure 5A). Proximity ligation assay confirmed the increased proximity between the 2 proteins during the same time interval (Figure 5B and 5C).

Immunostaining of uPARAP and VE-cadherin showed a colocalization, particularly in perinuclear areas, suggesting their potential interaction during endosomal trafficking. Subcellular localizations of protein complexes were detected by proximity ligation assay of uPARAP and VE-cadherin alongside immunostaining for Rab-GTPases (guanosine triphosphatases), which are markers of endosomes.[38] Molecular complexes were found in the Rab5$^+$ early endosome (Figure 5D) and the Rab11A$^+$ recycling endosome (Figure 5E), indicating their association during VE-cadherin trafficking.[39,40] These findings suggest that uPARAP may have a regulatory function in VE-cadherin endosomal transport, facilitating its recycling to the cell surface.

To investigate VE-cadherin internalization into Rab11A-positive endosomes, we conducted internalization assays. Cell-surface VE-cadherin was pulse-labeled, followed by VEGF-C stimulation and a low-pH wash to remove membrane-bound antibodies before cell fixation, leaving only internalized VE-cadherin for subsequent imaging (Figure 5F). In VEGF-C–treated control LECs, Rab11A$^+$ vesicles were dispersed throughout the cytoplasm. Pulsed VE-cadherin was mainly detected at the cell periphery, with minimal colocalization with Rab11A. In contrast, KD-LECs showed pulsed VE-cadherin predominantly within Rab11A$^+$ vesicles, suggesting increased VE-cadherin retention in the Rab11A$^+$ compartment in the absence of uPARAP. Moreover, closeness between VE-cadherin and Rab11A, initially detected in both control LECs and KD-LECs 10 minutes after VEGF-C stimulation, persisted 5 minutes longer in only KD-LECs (Figure 5G and 5H). These data highlight the regulatory role of uPARAP in VE-cadherin trafficking, specifically during recycling.

ROCK Inhibitor Reproduces the Labyrinthine Vasculature and Attenuates SL in vivo

Extensions and retractions of lamellipodia during cell junction turnover involve small Rho GTPases: Rac1 and RhoA (Ras homolog family member A), respectively.[37,41] Because Rac1 activation increases with uPARAP silencing[16] and ROCK (rho-associated coiled coil containing kinase) mediates RhoA activation, we used NSC 23766 Rac1 inhibitor to block lamellipodia formation and Y-27632 (ROCK inhibitor) to prevent membrane retraction. Our analysis focused on “overlapping junctions”

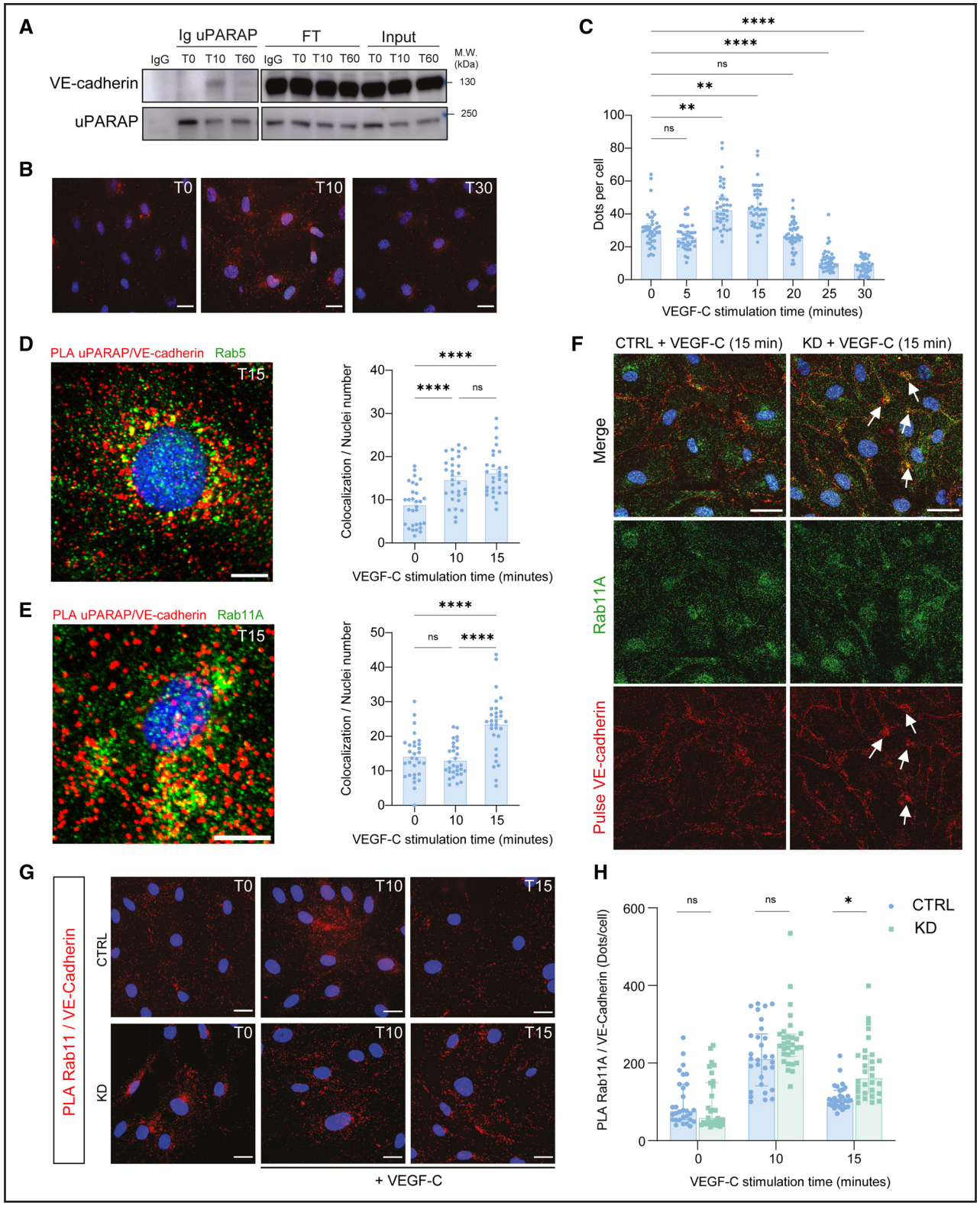

Figure 5. uPARAP interacts with vascular endothelial cadherin during its intracellular trafficking.
A, Immunoprecipitation of uPARAP (urokinase plasminogen activator receptor-associated protein) from lymphatic endothelial cells (LECs) stimulated with vascular endothelial growth factor–C (VEGF-C) for 0, 10, or 60 minutes (T0 to T60). Vascular endothelial (VE) cadherin and uPARAP protein levels were revealed by Western blot in immunoprecipitates, flowthrough (FT), and input samples. Control immunoprecipitation was performed with a mouse control antibody (immunoglobulin G). **B**, uPARAP/VE-cadherin complex was determined by proximity ligation assay (PLA) in LECs treated with VEGF-C during the indicated time (T, in minutes). **C**, Positive red dots of PLA VE-cadherin/uPARAP were quantified and normalized by nuclei count. Data are medians with interquartile ranges of 40 independent microscope fields by condition from 2 independent experiments. **D** and **E**, Representative images (**left**, at 15 minutes of VEGF-C stimulation) of Rab5 (**D**) or (*Continued*)

Figure 5 Continued. Rab11A (**E**; green) immunostainings conducted after PLA of uPARAP/VE-cadherin (red) in cells stimulated with VEGF-C. Quantification of the colocalization of PLA and immunostainings normalized by nuclei count are presented as mean±SEM of 10 independent microscope fields from 3 independent experiments. **F**, Immunolabeling of Rab11A was performed after pulse-chase assay in LECs silenced for uPARAP after VEGF-C stimulation (15 minutes). Cells were washed with acid buffer to remove cell surface VE-cadherin labeling. Arrows indicate VE-cadherin aggregates. **G** and **H**, PLA reveals Rab11A–VE-cadherin complex formation in control or knockdown (KD) LECs treated or not with VEGF-C for the indicated time (**G**). **H**, Quantification of red dots normalized by nuclei count from 10 independent microscope fields by condition and by experiment. Data are medians with interquartile ranges of 3 independent experiments. Scale bars=10 µm (**D** and **E**) or 20 µm (**C**, **F**, and **G**). Statistical tests: Kruskal-Wallis followed by Dunn test with Bonferroni correction (**C** and **H**) and 1-way ANOVA with Holm-Sidak post hoc test for multiple comparisons (**D** and **E**). *$P<0.05$; **$P<0.01$; ****$P<0.0001$.

(overlapping protrusions and wave-like lamellipodia) expanded by *uPARAP* knockdown and VEGF-C stimulation, corresponding to 51% of cell junctions (Figure 4C). Consistent with the role of Rac1 in promoting cell protrusion, NSC 23766 treatment led to 10.3% to 13.5% overlapping junctions in both control and KD-LECs, irrespective of VEGF-C (Figure 6A and 6B). Conversely, Y-27632–treated LECs displayed disrupted junctions under VEGF-C stimulation, resembling uPARAP silencing effects (Figure 6A and 6B). ROCK inhibition with VEGF-C stimulation also increased monolayer permeability in Boyden chambers (Figure 6C; $P<0.05$).

We hypothesized that a ROCK inhibitor could induce the labyrinthine lymphatic vasculature phenotype and reduce SL in vivo. Administration of ROCK inhibitor in SL WT mice reduced limb volume by 50% (Figure 6D) and increased lymphatic branching and tortuosity, forming a labyrinthine lymphatic vasculature (Figure 6E and 6F). LEC proliferation index remained unaffected by ROCK inhibition (Figure 6G). These results provide a proof of concept that generating a labyrinthine vasculature has the potential to attenuate SL (Figure 7A).

Computational Modeling Supports the Fluid-Absorbing Function for the Labyrinthine Lymphatic Vasculature

An in silico analysis was conducted to determine the drainage capacity of the normal hierarchical lymphatic vasculature observed in control or untreated mice and compare it with the labyrinthine vasculature observed in (global or conditional) *uparap*-deficient mice and in ROCK inhibitor–treated mice. Two-dimensional finite element models of dermis sections were implemented using poroelastic formulation to capture both solid and fluid phase behavior of the dermis. A computational model was designed to calculate the fluid pressure in the dermal tissue (excluding capillaries) under 0.02% horizontal and vertical compression, applied linearly for 10 seconds. This model was run on geometries derived from representative images of the lymphatic vasculature detected in both genetic mice (Figures 2A and 3E) and in ROCK inhibitor–treated mice (Figure 6E) under lymphedematous conditions (Figure 7B through 7D). In global and conditional $uparap^{-/-}$ mice ($uPARAP^{-/-}$ and $uPARAP^{\Delta LEC}$ mice), and in ROCK inhibitor–treated mice, all of which exhibited the labyrinthine vascular pattern, the average fluid pressures were substantially lower, reaching a 53% decrease in tissue pressure compared with their corresponding controls. Together, these in silico data support the observation of improved absorbing capacity of the labyrinthine topology featured by twisted and looped vessels compared with a normal hierarchical vasculature.

Gapmer Targeting of uparap Is a Therapeutic Option for SL

Gapmers consist of modified oligonucleotides flanking a central DNA segment, primarily linked by phosphorothioate bonds. We designed 5 gapmers (G1–G5) targeting uparap RNA and 1 gapmer control, each 16 nucleotides in length. Their efficacy was tested in mouse fibroblasts expressing uparap endogenously (Figure S6A and 6B). Transfection with G1, G2, G3, and G5 reduced uparap mRNA levels by 22% to 66.4%. G4 achieved higher and most sustained knockdown (72.4%±14.9 at 48 hours, 89.4%±5.8 at 72 hours, and 84.4%±3.5 at 96 hours; Figure S6A). Western blotting analysis confirmed reduced uPARAP protein levels with all tested gapmers, with G4 inducing an almost complete uPARAP loss (Figure S6B). Four repeated doses of G4 were then subcutaneously administered to mice subjected to SL (Figure 8A). In contrast to control gapmer, G4 reduced limb swelling (Figure 8A) and accumulation of adipocytes and their size (Figure S6C and S6D). G4-treated mice exhibited the atypical lymphatic vasculature with increased tortuosity and hyperbranching (Figure 8C and 8D) versus untreated or control gapmer–treated mice. G4 administration did not affect the epidermal/dermal thickenings (Figure 8B), proliferation index (Figure 8E), or macrophage-associated inflammation (Figure S6E). We observed a modest effect of the control gapmer on macrophage infiltration in control and SL skins. These data demonstrate that the delivery of anti-uparap gapmers is efficient to attenuate SL development and may represent a novel therapeutic approach for SL treatment.

Considering that uPARAP effects on LEC phenotype are dependent on VEGF-C stimulation, we investigated whether inhibiting VEGF-C could counteract gapmer effects. We used AAVs encoding a soluble VEGF-C trap (AAV-VEGFR-3[1-3]-IgG-Fc)[18] or nonligand binding region of VEGFR-3 extracellular domain (AAV-VEGFR-3[4-7]-IgG-Fc)[19] as a control. The therapeutic effect of G4 on SL was reversed by VEGF-C trap administration,

 Circulation. 2025;151:1412–1429. DOI: 10.1161/CIRCULATIONAHA.124.072093

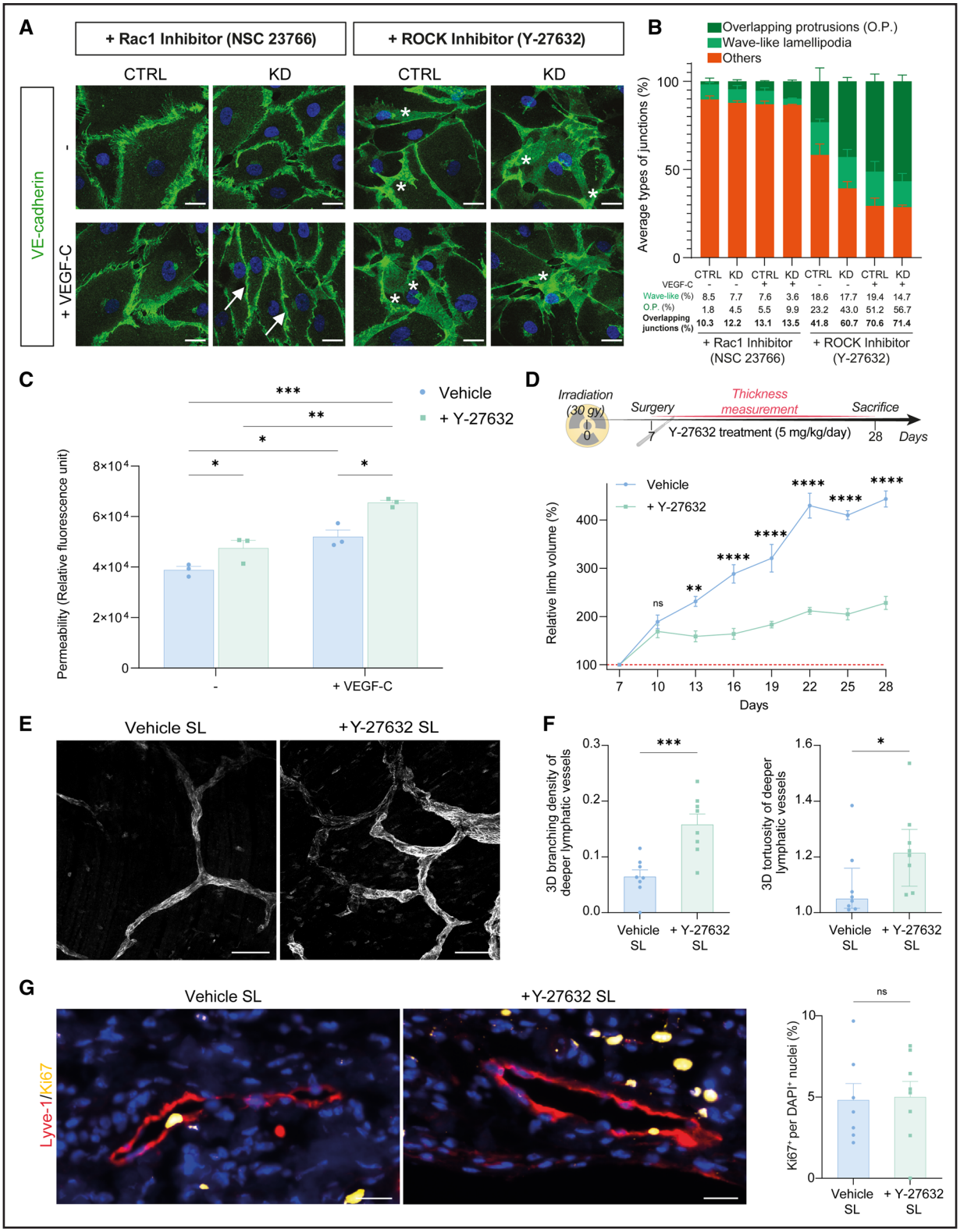

Figure 6. Rac1 and ROCK inhibitors recapitulate uPARAP silencing effects on cell overlapping in vitro and ROCK inhibitor induces a labyrinthine vasculature with attenuated secondary lymphedema in vivo.

A and **B**, Control or knockdown (KD) cells were treated with either Rac1 (Ras-related C3-rich protein 1) inhibitor (NSC 23766) or ROCK (rho-associated coiled coil containing kinase) inhibitor (Y-27632) for 1 hour followed by vascular endothelial growth factor–C (VEGF-C) stimulation for 2 hours. Overlapping junctions (wave-like + overlapping protrusions [OP], as in Figure 3) and other types of junctions were quantified after vascular endothelial (VE) cadherin immunostaining (green). Scale bars=20 μm. Data are mean±SEM (**B**). **C**, Relative permeability of FITC-dextran (40 kDa) assessed after 75 minutes in lymphatic endothelial cells (LECs) treated or not with ROCK inhibitor, stimulated or not with (*Continued*)

Figure 6 Continued. VEGF-C. Data are mean±SEM from 3 independent experiments. **D**, Timeline of secondary lymphedema (SL) induction in wild-type mice untreated (vehicle; n=8) or treated with ROCK (Y-27632) inhibitor (n=8). Representative follow-up of the relative volume of the limb. Results are expressed as percentage of control limb volume (100%; dotted line). Data are mean±SEM. **E**, Z-stack projections of deeper Lyve-1–positive lymphatic vessels in SL skin. Scale bars=250 µm. **F**, Three-dimensional quantification of deeper Lyve-1–positive vessels in whole-mount SL skin samples of vehicle and Y-27632–treated mice. The 2 graphs correspond to 3-dimensional (3D) branching density (left) and 3D tortuosity (right). Data are mean±SEM (**F**, left) or median and interquartile range (**F**, right). **G**, Representative images (left) and quantification (right) of Ki67$^+$ (yellow) per DAPI$^+$ (blue) nuclei in deeper Lyve-1–positive vessels (red) of lymphedema skins in ROCK inhibitor treated or untreated mice. Scale bar=20 µm. Data are mean±SEM. Statistical tests: 2-way ANOVA (**C**), 2-way repeated-measures ANOVA (**D**), both with Holm-Sidak post hoc test for multiple comparisons; unpaired *t* test (**F** in left graph, **G**); and Mann-Whitney *U* test (**F** in right graph). **P*<0.05; ***P*<0.01; ****P*<0.001; *****P*<0.0001.

but not by control AAV-VEGFR-3(4-7)-IgG-Fc injection (Figure 8F). These findings indicate that the therapeutic effect of G4 is dependent on VEGF-C.

DISCUSSION

We discovered that both global and LEC-specific genetic deletion of *uparap* in SL mice results in atypical lymphatic vessels, characterized as a labyrinthine vasculature with hyperbranched and twisted vessels and reduction of SL severity. A similar vascular pattern and SL attenuation was reproduced by using a pharmacologic ROCK inhibitor, a finding worth further consideration in the context of lymphedema. Our study uncovers a pivotal role for uPARAP in regulating VE-cadherin–mediated cell junctions in lymphatic vessels. We also show that in vivo uparap downregulation using a gapmer approach offers a novel therapeutic concept for lymphedema treatment.

Our previous work showed that uPARAP, an endocytic receptor involved in intracellular collagen degradation, is a regulator of VEGF-C–mediated lymphangiogenesis.[16] We then considered that uPARAP, acting at the interface between collagen remodeling and lymphatic vessel formation, could modulate SL formation through either or both of these properties. To clarify the function of uPARAP in SL, we used a preclinical model of cancer-related SL that replicates its key pathologic features, such as limb swelling, epidermal/dermal thickening, lymphatic remodeling, inflammation, adipocyte accumulation, and fibrosis.[17] Genetic ablation of *uparap* significantly reduced limb swelling, epidermal thickening, and adipocyte accumulation and size. This was linked to the atypical labyrinthine lymphatic vasculature, which was composed of predominantly precollecting Lyve-1$^+$ vessels with α–smooth muscle actin$^+$ cell coverage and valves. Although lymphatic valves were not altered, such a vascular pattern may contribute to SL attenuation through the contractile functions of the associated smooth muscle cells. Moreover, the presence of valves cannot be ruled out in some of the atypical cell junctions observed in *uparap*$^{-/-}$ SL skins. The SL mitigation was not attributed to the collagen endocytic function of uPARAP, because collagen remodeling was not significantly different in SL skins of *uparap*$^{-/-}$ mice versus *uparap*$^{+/+}$ mice. Furthermore, specific deletion of *uparap* in LECs phenocopied the labyrinthine pattern associated with reduced SL, further confirming the LEC-specific effect of uPARAP. A disorganized LEC arrangement was found within the labyrinthine vasculature of *uparap*$^{-/-}$ mice, and this was replicated in another experimental murine model of VEGF-C–driven lymphangiogenesis (ear injection; Figure 2D). Consistent findings were reproduced in vitro in KD-LECs and associated with increased permeability of the LEC monolayer under VEGF-C stimulation. These data indicate a key contribution of uPARAP in shaping lymphatic vessels under pathologic conditions. In contrast, our previous findings indicated that *uparap* deficiency did not affect the physiologic or postnatal development of the cutaneous lymphatic network,[16] suggesting a therapeutic window for targeting only the lymphatic vessels in SL. We cannot exclude an effect of sex on uPARAP function in SL, because only female mice were used in the study.

Key findings surfaced through in-depth analyses of VE-cadherin trafficking in siRNA-mediated *uPARAP*-silenced human primary LECs (KD-LECs). We provide evidence that uPARAP interacts transiently with VE-cadherin after VEGF-C stimulation. uPARAP/VE-cadherin complexes were first detected in Rab5$^+$ early endosomes and then in Rab11A$^+$ recycling vesicles. uPARAP promoted the smooth recycling of VE-cadherin to the cell surface, whereas its silencing induced VE-cadherin retention in Rab11$^+$ vesicles. This revealed an intriguing novel facet of uPARAP involvement in LEC junction dynamics, extending its roles beyond matrix remodeling, cell migration,[12–14] and VEGF-C–driven lymphangiogenesis.[16] The capacity of uPARAP to modulate VEGFR-2/VEGFR-3 heterodimerization and downstream signaling may also contribute to VE-cadherin phosphorylation and subsequent internalization.[16,42–45] However, in control and KD-LECs, we found similar phosphorylation levels of VE-cadherin (on Y658 and Y685). Thus, uPARAP orchestrates the rapid recycling of VE-cadherin for the establishment of new adherens junctions, without affecting its phosphorylation level.

Exacerbated "overlapping junctions" in KD-LECs, including wave-like lamellipodia and overlapping protrusions, are likely to be related to the transient JAIL process described in blood endothelial cells, but not in LECs.[41,46] Key features regulating JAIL dynamics are local VE-cadherin concentration and activity of small GTPases, wherein Rac1 contributes to lamellipodia protrusion

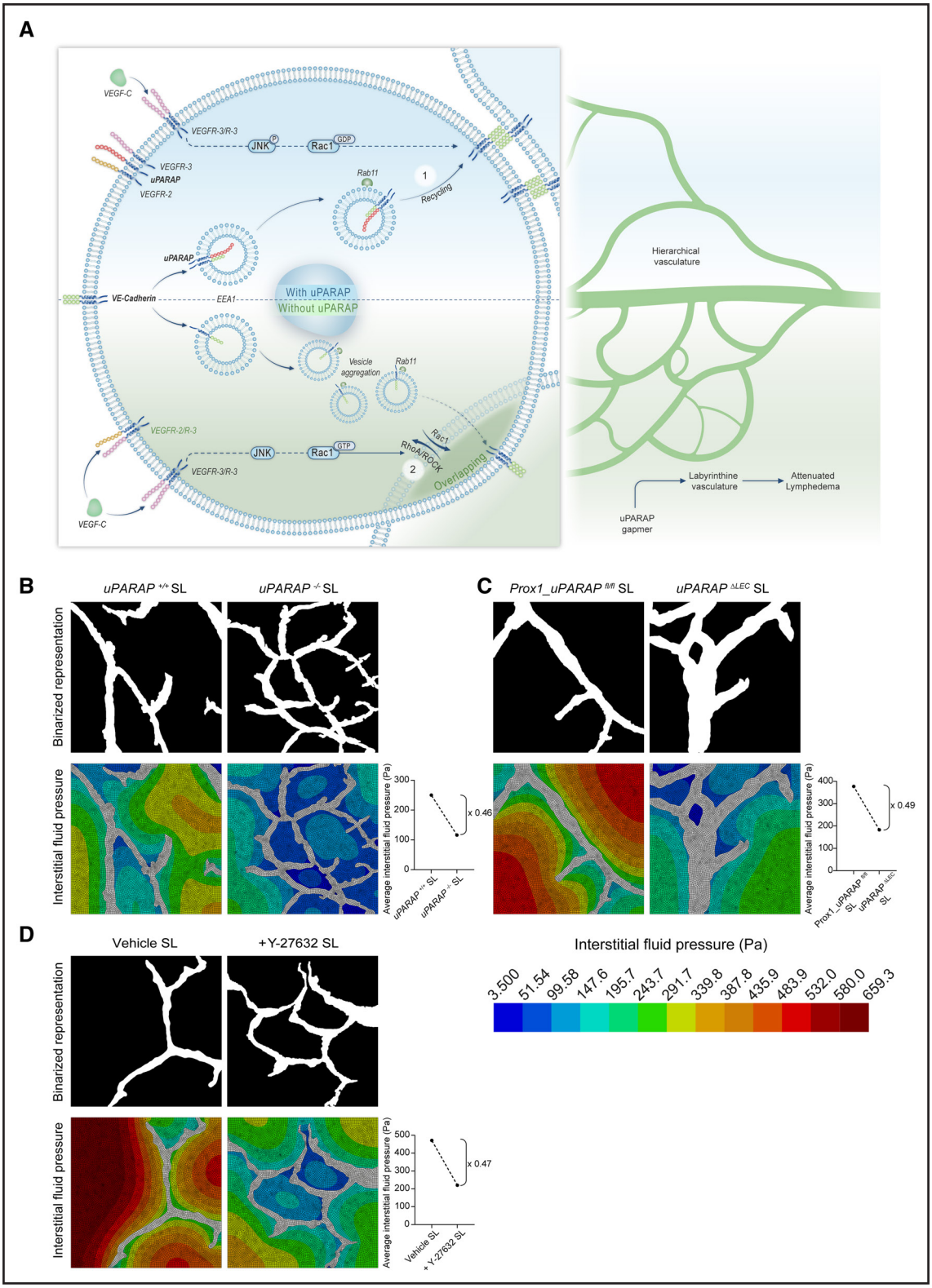

Figure 7. In silico simulation of fluid absorption in different topologies of the lymphatic vasculature.
A, Schematic representation of the proposed model of labyrinthine vasculature. The reestablishment of lymphatic endothelial cell (LEC)–LEC junctions upon vascular endothelial growth factor–C (VEGF-C) stimulation relies on the correct endosomal trafficking of VE-cadherin and small GTPase activities (Rac1 [Ras-related C3-rich protein 1] for the formation of protrusions and ROCK [rho-associated coiled coil containing kinase]/RhoA (Ras homolog family member A) for their retraction). (Top) uPARAP (urokinase plasminogen activator receptor-associated protein) binds to VE-cadherin in early endosomes (EEA1) and drives it to Rab11$^+$ recycling endosomes for its return to the cell surface. uPARAP also reduces VEGFR-2/VEGFR-3 heterodimerization, leading to increased Rac1 activity (Rac1-GTP).[16] In the presence of uPARAP, appropriate (*Continued*)

Figure 7 Continued. VE-cadherin concentration and Rac1 activity promote the elaboration of a hierarchical vasculature with linear cell junctions. (Bottom) In the absence of uPARAP, VE-cadherin persists in recycling Rab11$^+$ vesicles. The lower concentration of VE-cadherin at the cell surface, together with reduced Rac1 activity, lead to a labyrinthine vascular network with overlapping cells. This labyrinthine vasculature associated with attenuated lymphedema can be reproduced by ROCK inhibition or uPARAP downregulation via gapmers. **B** through **D**, A computational model was designed to calculate the interstitial fluid pressure and run on geometries derived from the original in vivo images of deeper lymphatic vessels from SL tissues. The model was run at either basal or high permeability. Images display the interstitial pressures around lymphatic vessels for each experimental condition. The levels of interstitial fluid pressure generated after 10 seconds of simulation are illustrated by a color panel (color scale ranging from 10 to 170 Pa). The graphs correspond to the average interstitial pressures in *uparap*-deficient or inhibitor-treated mice, as compared with their corresponding controls. **B**, uPARAP$^{+/+}$ and uPARAP$^{-/-}$ mice (corresponding to Figure 2A). **C**, *Prox1_uPARAP$^{fl/fl}$* and *uPARAP$^{\Delta LEC}$* mice (corresponding to Figure 3E). **D**, Vehicle-treated and Y-27632 (ROCK)–treated mice (corresponding to Figure 6E).

and RhoA/ROCK to their retraction.[37,41] Involvement of JAIL in our so-called overlapping phenotype observed in *uPARAP*-silenced LECs is supported by the following features: VE-cadherin staining pattern (clustering) in wave-like lamellipodia, low rate of VE-cadherin recycling at the cell surface, and Rac1/ROCK involvement in retraction of cell extensions assessed by pharmacologic approaches. Furthermore, we previously demonstrated that uPARAP also regulates Rac1 activity.[16]

Our data converge toward a novel model in which an atypical lymphatic vascular network formed by hyperbranched and twisted vessels with altered cell–cell junctions reduces SL severity. Pharmacologic inhibition of ROCK was used to validate this concept. ROCK inhibition altered VE-cadherin–mediated LEC monolayer integrity and permeability in vitro and induced the formation of an abnormal lymphatic network in vivo. Hence, it reproduced a similar labyrinthine vasculature and reduced SL in vivo. The effect of ROCK inhibitor on LEC proliferation in vivo is distinct from that of *uparap* deficiency, likely because only uPARAP modulates the VEGFR-2/VEGFR-3 pathway. Beyond providing a proof of concept, our findings also provide new mechanistic insights into the functionality of ROCK inhibitors in VE-cadherin–mediated cell–cell junctions, elucidating how they can mitigate SL in vivo.[47]

It may appear counterintuitive that a complex network of twisted and hyperpermeable vessels could improve lymphatic drainage. However, such a labyrinthine vasculature could facilitate lymphatic drainage through various mechanisms. First, the hyperpermeability of these vessels improves fluid intravasation into the lymphatic vasculature. Next, the twisted nature of the vessels increases the drainage surface area, enhancing the efficiency of fluid removal. In addition, the intricate branching and looping of lymphatics provide multiple alternative pathways for fluid transport, which is particularly beneficial in cases where luminal obstruction occurs, such as in patients with SL.[48] Based on in vitro and in vivo results highlighting alterations in cell–cell junctions involved in fluid intravasation, we generated an in silico model simulating interstitial fluid removal. Our in silico approach used authentic and binarized images generated in vivo in the genetically modified or pharmacologically treated mice. This computational modeling confirmed the notion of improved fluid-absorbing function of the labyrinthine vascular pattern as compared with the classic hierarchical one.

Chronic lymphatic dysfunction affects millions of people worldwide. Despite recent important advances in the field of lymphatic biology, patients with lymphedema need more effective therapy. We provide evidence that uPARAP is a therapeutic target that is worth considering for the design of future treatment. We thus decided to use gapmers (ie, antisense oligonucleotides) to selectively downregulate uparap. This innovative approach aims to inhibit the translation of the target gene product.[49] Their structure ensures both specificity for the target and drug stability, which are more difficult to obtain with siRNAs. Another advantage of gapmer technology is to overcome the issue of safety that might be related to viral vectors used, for instance, when delivering short hairpin RNAs. The use of gapmers holds promise in the clinic and some of them (eg, mipomersen, inotersen, eteplirsen, golodirsen) have been approved by the Food and Drug Administration for the treatment of genetic diseases.[50] Subcutaneous administration of a gapmer targeting uparap successfully induced a labyrinthine vasculature and attenuated SL. The slight reduction of epidermal thickening achieved with genetic ablation of *uparap* was not detected with anti-uparap gapmer. This might be related to the early induction of the epidermal thickening that cannot be modulated by gapmers, which were injected at a later time point.

Our study underscores the potential of targeting uPARAP to promote lymphatic remodeling and to attenuate lymphedema. The role of VEGF-C in uPARAP function was supported by the use of a VEGF-C trap, which blocked the effects of anti-uparap gapmers. Collectively, our findings suggest that the labyrinthine vasculature and attenuated SL observed in the *uparap$^{-/-}$* mice result from multiple VEGF-C–driven lymphovascular properties of uPARAP. These include regulation of VEGFR-3 downstream signaling that triggers lymphangiogenesis and impairs directional LEC migration,[16] modulation of Rac1 activity,[16] and control of VE-cadherin trafficking.

The intricate features of the labyrinthine vasculature formed of precollecting vessels appear well-suited for improvement of lymphatic drainage in SL. Understanding the multifaceted roles of proteins such as uPARAP and ROCK in this context not only sheds light on their

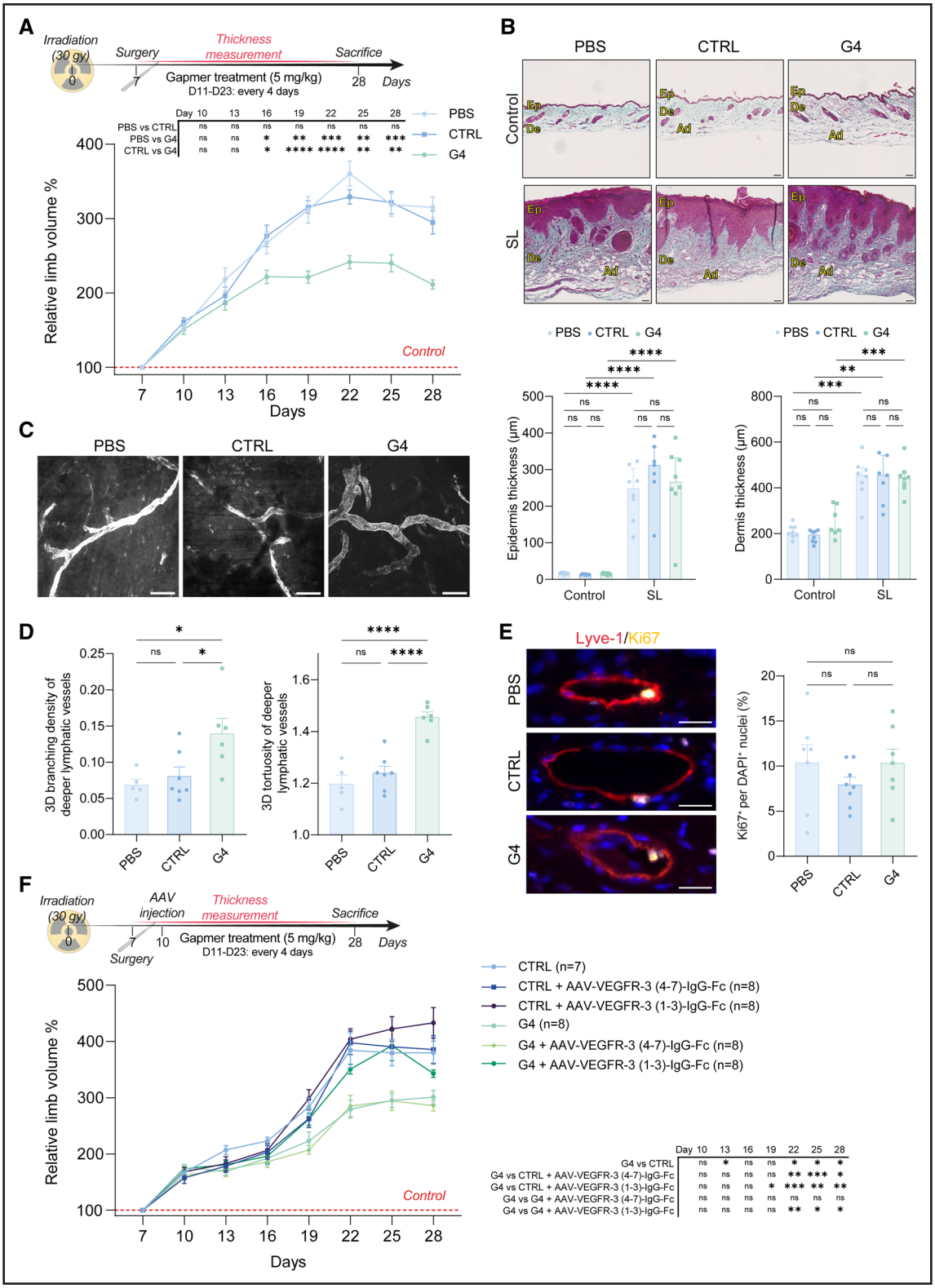

Figure 8. An anti-uparap gapmer induces labyrinthine vasculature with attenuated secondary lymphedema in vivo.
A, Timeline of secondary lymphedema (SL) induction in wild-type mice treated with a gapmer (G4) targeting uparap (urokinase plasminogen activator receptor-associated protein; n=8), a negative control gapmer (control; n=8), or PBS (n=8). The graph corresponds to the follow-up of the relative volume of the limb (percentage of control limb volume; dotted line=100%). Data are mean±SEM. **B**, Representative images of skin sections stained with Masson trichrome (above). Epidermis (Ep), dermis (De), and adipocytes (Ad) are delineated. Scale bars=50 µm. Graphs represent quantification of epidermal thickness (left) and dermis thickness (right) in SL and control skins. Data are mean±SEM. **C**, Z-stack projections of deeper Lyve-1$^+$ lymphatic vessels in lymphedema skin. Scale bars=250 µm. **D**, Three-dimensional quantification of deeper Lyve-1$^+$ vessels in whole-mounted SL skin samples: 3-dimensional branching density (left) and 3-dimensional tortuosity (right) as evaluated in (*Continued*)

Figure 8 Continued. Figures 2B, 3F, and 6F. **E**, Representative images (left) and quantification (right) of Ki67$^+$ (yellow) per DAPI$^+$ (blue) nuclei in deeper Lyve-1$^+$ vessels (red) of lymphedema skins: PBS, control, and G4-treated mice. Ki67$^+$ nuclei were quantified as in Figure 1G. Scale bar=20 µm. Data are mean±SEM. **F**, Timeline of SL induction in wild-type mice treated with G4 gapmer, or control gapmer (control) with or without vascular endothelial growth factor–C (VEGF-C) trap (adeno-associated virus [AAV]-VEGFR-3[1-3]-IgG-Fc) or control AAV (AAV-VEGFR-3[4-7]-IgG-Fc; n≥7 for all groups). Results are expressed as in **A**. Statistical tests: 2-way repeated-measures ANOVA (**A** and **F**) and 2-way ANOVA (**B**) with Holm-Sidak post hoc test for multiple comparisons and 1-way ANOVA with Holm-Sidak post hoc test for multiple comparisons (**D** and **E**). *P<0.05; **P<0.01; ***P<0.001; ****P<0.0001.

functions in lymphatic pathophysiology, but also holds promise for therapeutic reshaping of the lymphatic vasculature to facilitate fluid removal in the lymphedematous context. Our findings provide evidence that targeting uPARAP offers a novel therapeutic option for lymphedema.

ARTICLE INFORMATION

Received September 02, 2024; accepted February 4, 2025.

Affiliations

From the Laboratory of Tumor and Development Biology, GIGA (F.G., A.L., S.P., F.B., E.I., S.B., J.D., L.B., A.P., C.M., M.G.-I., A.N.), and Departments of Plastic and Reconstructive Surgery (C.N.) and Radiotherapy-Oncology (F.L.), University of Liège, Sart-Tilman, Belgium. Human Molecular Genetics, de Duve Institute, University of Louvain, Brussels, Belgium (P.B., M.V.). U1297-Institut des Maladies Métaboliques et Cardiovasculaires (I2MC), Institut National de la Santé et de la Recherche Médicale (INSERM), Université de Toulouse, France (F.M.). Biomechanics Research Unit Department, Skeletal Biology and Engineering Research Center, Department of Development and Regeneration, KU Leuven, Belgium (C.V., L.G.). WELBIO Department, WEL Research Institute, Wavre, Belgium (M.V., A.N.). Wihuri Research Institute and Translational Cancer Medicine Program, Biomedicum, University of Helsinki, Finland (K.A.).

Acknowledgments

The authors thank Emilie Feyereisen, Isabelle Dasoul, Erika Konradowski, Laetitia Montero-Ruiz, and Nathalie Lefin for technical support; and Animascience for elaboration of the graphical abstract. GIGA platforms (GIGA–Cell Imaging, GIGA–Viral Vectors, and GIGA–Mouse Facility) were used in this study. All figure rights have been transferred to the authors.

Sources of Funding

This work was supported by grants from the Walloon Region through the FRFS-WELBIO strategic research program (WELBIO-CR-2019A–03R to Dr Noel; WELBIO-IP X1548.24 to Dr Vikkula), the Fonds de la Recherche Scientifique–FNRS (FRS-FNRS, Belgium) T.0240.23 and P.C005.22 (to Dr Vikkula), the Fondation Contre le Cancer (Foundation of Public Interest, Belgium), the Fonds Spéciaux de la Recherche (University of Liège), the Centre Anticancéreux près l'Université de Liège, the Fonds Léon Fredericq (University of Liège), the PROTHERWAL project 7289 from the "Direction Générale Opérationnelle de l'Economie," and the Wallonia-Brussels Federation (grant for Concerted Research Actions). This project has received funding from the European Union Horizon 2020 research aid innovation program under grant agreement 874708 (Theralymph). Dr Gucciardo and J. Deroye are supported by a FRS-FNRS-Télévie grant. Dr Brouillard is a Scientific Logistics Manager of the Genomics Platform of the University of Louvain.

Disclosures

None.

Supplemental Material

Methods

Figures S1–S6

Videos S1 and S2

REFERENCES

1. Rockson SG. Advances in lymphedema. *Circ Res*. 2021;128:2003–2016. doi: 10.1161/CIRCRESAHA.121.318307
2. Brouillard P, Witte MH, Erickson RP, Damstra RJ, Becker C, Quéré I, Vikkula M. Primary lymphoedema. *Nat Rev Dis Primer*. 2021;7:1–23. doi: 10.1038/s41572-021-00309-7
3. Dixelius J, Mäkinen T, Wirzenius M, Karkkainen MJ, Wernstedt C, Alitalo K, Claesson-Welsh L. Ligand-induced vascular endothelial growth factor receptor-3 (VEGFR-3) heterodimerization with VEGFR-2 in primary lymphatic endothelial cells regulates tyrosine phosphorylation sites. *J Biol Chem*. 2003;278:40973–40979. doi: 10.1074/jbc.M304499200
4. Nilsson I, Bahram F, Li X, Gualandi L, Koch S, Jarvius M, Söderberg O, Anisimov A, Kholová I, Pytowski B, et al. VEGF receptor 2/-3 heterodimers detected in situ by proximity ligation on angiogenic sprouts. *EMBO J*. 2010;29:1377–1388. doi: 10.1038/emboj.2010.30
5. Secker GA, Harvey NL. VEGFR signaling during lymphatic vascular development: From progenitor cells to functional vessels. *Dev Dyn*. 2015;244:323–331. doi: 10.1002/dvdy.24227
6. Brouillard P, Boon L, Vikkula M. Genetics of lymphatic anomalies. *J Clin Invest*. 2014;124:898–904. doi: 10.1172/JCI71614
7. Saaristo A, Tammela T, Timonen J, Yla-Herttuala S, Tukiainen E, Asko-Seljavaara S, Alitalo K. Vascular endothelial growth factor-C gene therapy restores lymphatic flow across incision wounds. *FASEB J*. 2004;18:1707–1709. doi: 10.1096/fj.04-1592fje
8. Baik JE, Park HJ, Kataru RP, Savetsky IL, Ly CL, Shin J, Encarnacion EM, Cavali MR, Klang MG, Riedel E, et al. TGF-β1 mediates pathologic changes of secondary lymphedema by promoting fibrosis and inflammation. *Clin Transl Med*. 2022;12:e758. doi: 10.1002/ctm2.758
9. Brown S, Campbell AC, Kuonqui K, Sarker A, Park HJ, Shin J, Kataru RP, Coriddi M, Dayan JH, Mehrara BJ. The future of lymphedema: potential therapeutic targets for treatment. *Curr Breast Cancer Rep*. 2023;15:233–241. doi: 10.1007/s12609-023-00491-5
10. Nguyen DH, Zhou A, Posternak V, Rochlin DH. Nanofibrillar collagen scaffold enhances edema reduction and formation of new lymphatic collectors after lymphedema surgery. *Plast Reconstr Surg*. 2021;148:1382–1393. doi: 10.1097/PRS.0000000000008590
11. Leppäpuska I-M, Hartiala P, Suominen S, Suominen E, Kaartinen I, Mäki M, Seppänen M, Kiiski J, Viitanen T, Lahdenperä O, et al. Phase 1 Lymfactin study: 24-month efficacy and safety results of combined adenoviral VEGF-C and lymph node transfer treatment for upper extremity lymphedema. *J Plast Reconstr Aesthet Surg*. 2022;75:3938–3945. doi: 10.1016/j.bjps.2022.08.011
12. Melander MC, Jürgensen HJ, Madsen DH, Engelholm LH, Behrendt N. The collagen receptor uPARAP/Endo180 in tissue degradation and cancer (review). *Int J Oncol*. 2015;47:1177–1188. doi: 10.3892/ijo.2015.3120
13. Sturge J. Endo180 at the cutting edge of bone cancer treatment and beyond. *J Pathol*. 2016;238:485–488. doi: 10.1002/path.4673
14. Gucciardo F, Pirson S, Baudin L, Lebeau A, Noël A. uPARAP/Endo180: a multifaceted protein of mesenchymal cells. *Cell Mol Life Sci*. 2022;79:255. doi: 10.1007/s00018-022-04249-7
15. Engelholm LH, Ingvarsen S, Jürgensen HJ, Hillig T, Madsen DH, Nielsen BS, Behrendt N. The collagen receptor uPARAP/Endo180. *Front Biosci (Landmark Ed)*. 2009;14:2103–2114. doi: 10.2741/3365
16. Durré T, Morfoisse F, Erpicum C, Ebroin M, Blacher S, García-Caballero M, Deroanne C, Louis T, Balsat C, Van de Velde M, et al. uPARAP/Endo180 receptor is a gatekeeper of VEGFR-2/VEGFR-3 heterodimerisation during pathological lymphangiogenesis. *Nat Commun*. 2018;9:5178. doi: 10.1038/s41467-018-07514-1
17. Buntinx F, Lebeau A, Gillot L, Baudin L, Ndong Penda R, Morfoisse F, Lallemand F, Vottero G, Nizet C, Nizet JL, et al. Single and combined impacts of irradiation and surgery on lymphatic vasculature and fibrosis associated to secondary lymphedema. *Front Pharmacol*. 2022;13:1016138. doi: 10.3389/fphar.2022.1016138
18. Fang S, Nurmi H, Heinolainen K, Chen S, Salminen E, Saharinen P, Mikkola HKA, Alitalo K. Critical requirement of VEGF-C in transition to fetal erythropoiesis. *Blood*. 2016;128:710–720. doi: 10.1182/blood-2015-12-687970
19. Alitalo AK, Proulx ST, Karaman S, Aebischer D, Martino S, Jost M, Schneider N, Bry M, Detmar M. VEGF-C and VEGF-D blockade inhibits

inflammatory skin carcinogenesis. *Cancer Res*. 2013;73:4212–4221. doi: 10.1158/0008-5472.CAN-12-4539
20. Gommes CJ, Bons A-J, Blacher S, Dunsmuir JH, Tsou AH. Practical methods for measuring the tortuosity of porous materials from binary or gray-tone tomographic reconstructions. *AIChE J*. 2009;55:2000–2012. doi: 10.1002/aic.11812
21. Pacchiana R, Abbate M, Armato U, Dal Prà I, Chiarini A. Combining immunofluorescence with in situ proximity ligation assay: a novel imaging approach to monitor protein-protein interactions in relation to subcellular localization. *Histochem Cell Biol*. 2014;142:593–600. doi: 10.1007/s00418-014-1244-8
22. Dorland YL, Malinova TS, van Stalborch A-MD, Grieve AG, van Geemen D, Jansen NS, de Kreuk B-J, Nawaz K, Kole J, Geerts D, et al. The F-BAR protein pacsin2 inhibits asymmetric VE cadherin internalization from tensile adherens junctions. *Nat Commun*. 2016;7:12210. doi: 10.1038/ncomms12210
23. Neto F, Klaus-Bergmann A, Ong YT, Alt S, Vion A-C, Szymborska A, Carvalho JR, Hollfinger I, Bartels-Klein E, Franco CA, et al. YAP and TAZ regulate adherens junction dynamics and endothelial cell distribution during vascular development. *eLife*. 2018;7:e31037. doi: 10.7554/eLife.31037
24. Gavard J, Gutkind JS. VEGF controls endothelial-cell permeability by promoting the beta-arrestin-dependent endocytosis of VE cadherin. *Nat Cell Biol*. 2006;8:1223–1234. doi: 10.1038/ncb1486
25. Li R, Ren M, Chen N, Luo M, Zhang Z, Wu J. Vitronectin increases vascular permeability by promoting VE cadherin internalization at cell junctions. *PLoS One*. 2012;7:e37195. doi: 10.1371/journal.pone.0037195
26. Detournay E, Cheng AH-D. Fundamentals of poroelasticity. In: Fairhurst C, ed. *Analysis and Design Methods*. Pergamon; 1993:113–171. doi: 10.1016/B978-0-08-040615-2.50011-3
27. Biot MA. General theory of three-dimensional consolidation. *J Appl Phys*. 1941;12:155–164. doi: 10.1063/1.1712886
28. Villette CC, Phillips ATM. Informing phenomenological structural bone remodelling with a mechanistic poroelastic model. *Biomech Model Mechanobiol*. 2016;15:69–82. doi: 10.1007/s10237-015-0735-4
29. Pereira AF, Shefelbine SJ. The influence of load repetition in bone mechanotransduction using poroelastic finite-element models: the impact of permeability. *Biomech Model Mechanobiol*. 2014;13:215–225. doi: 10.1007/s10237-013-0498-8
30. Kameo Y, Adachi T. Modeling trabecular bone adaptation to local bending load regulated by mechanosensing osteocytes. *Acta Mech*. 2014;225:2833–2840. doi: 10.1007/s00707-014-1202-5
31. Oftadeh R, Azadi M, Donovan M, Langer J, Liao I-C, Ortiz C, Grodzinsky AJ, Luengo GS. Poroelastic behavior and water permeability of human skin at the nanoscale. *PNAS Nexus*. 2023;2:pgad240. doi: 10.1093/pnasnexus/pgad240
32. Leng Y, Wang H, de Lucio M, Gomez H. Mixed-dimensional multiscale poroelastic modeling of adipose tissue for subcutaneous injection. *Biomech Model Mechanobiol*. 2022;21:1825–1840. doi: 10.1007/s10237-022-01622-0
33. Sachs D, Wahlsten A, Kozerke S, Restivo G, Mazza E. A biphasic multilayer computational model of human skin. *Biomech Model Mechanobiol*. 2021;20:969–982. doi: 10.1007/s10237-021-01424-w
34. Huxley VH, Meyer DJ. Capillary permeability: atrial peptide action is independent of "protein effect." *Am J Physiol*. 1990;259:H1351–H1356. doi: 10.1152/ajpheart.1990.259.5.H1351
35. Swartz MA, Kaipainen A, Netti PA, Brekken C, Boucher Y, Grodzinsky AJ, Jain RK. Mechanics of interstitial-lymphatic fluid transport: theoretical foundation and experimental validation. *J Biomech*. 1999;32:1297–1307. doi: 10.1016/s0021-9290(99)00125-6
36. Peña-Jimenez D, Fontenete S, Megias D, Fustero-Torre C, Graña-Castro O, Castellana D, Loewe R, Perez-Moreno M. Lymphatic vessels interact dynamically with the hair follicle stem cell niche during skin regeneration in vivo. *EMBO J*. 2019;38:e101688. doi: 10.15252/embj.2019101688
37. Cao J, Ehling M, März S, Seebach J, Tarbashevich K, Sixta T, Pitulescu ME, Werner A-C, Flach B, Montanez E, et al. Polarized actin and VE cadherin dynamics regulate junctional remodelling and cell migration during sprouting angiogenesis. *Nat Commun*. 2017;8:2210. doi: 10.1038/s41467-017-02373-8
38. Homma Y, Hiragi S, Fukuda M. Rab family of small GTPases: an updated view on their regulation and functions. *FEBS J*. 2021;288:36–55. doi: 10.1111/febs.15453
39. Barbieri MA, Roberts RL, Mukhopadhyay A, Stahl PD. Rab5 regulates the dynamics of early endosome fusion. *Biocell*. 1996;20:331–338.
40. Green EG, Ramm E, Riley NM, Spiro DJ, Goldenring JR, Wessling-Resnick M. Rab11 is associated with transferrin-containing recycling compartments in K562 cells. *Biochem Biophys Res Commun*. 1997;239:612–616. doi: 10.1006/bbrc.1997.7520
41. Cao J, Schnittler H. Putting VE cadherin into JAIL for junction remodeling. *J Cell Sci*. 2019;132:jcs222893. doi: 10.1242/jcs.222893
42. Dejana E, Orsenigo F, Lampugnani MG. The role of adherens junctions and VE cadherin in the control of vascular permeability. *J Cell Sci*. 2008;121:2115–2122. doi: 10.1242/jcs.017897
43. Orsenigo F, Giampietro C, Ferrari A, Corada M, Galaup A, Sigismund S, Ristagno G, Maddaluno L, Young Koh G, Franco D, et al. Phosphorylation of VE cadherin is modulated by haemodynamic forces and contributes to the regulation of vascular permeability in vivo. *Nat Commun*. 2012;3:1–15. doi: 10.1038/ncomms2199
44. Sun Z, Li X, Massena S, Kutschera S, Padhan N, Gualandi L, Sundvold-Gjerstad V, Gustafsson K, Choy WW, Zang G, et al. VEGFR2 induces c-Src signaling and vascular permeability in vivo via the adaptor protein TSAD. *J Exp Med*. 2012;209:1363–1377. doi: 10.1084/jem.20111343
45. Gavard J. Endothelial permeability and VE cadherin: a wacky comradeship. *Cell Adh Migr*. 2013;7:455–461. doi: 10.4161/cam.27330
46. Seebach J, Klusmeier N, Schnittler H. Autoregulatory "multitasking" at endothelial cell junctions by junction-associated intermittent lamellipodia controls barrier properties. *Front Physiol*. 2020;11:586921. doi: 10.3389/fphys.2020.586921
47. Lee E, Chan S-L, Lee Y, Polacheck WJ, Kwak S, Wen A, Nguyen DT, Kutys ML, Alimperti S, Kolarzyk AM, et al. A 3D biomimetic model of lymphatics reveals cell–cell junction tightening and lymphedema via a cytokine-induced ROCK2/JAM-A complex. *Proc Natl Acad Sci USA*. 2023;120:e2308941120. doi: 10.1073/pnas.2308941120
48. Mihara M, Hara H, Hayashi Y, Narushima M, Yamamoto T, Todokoro T, Iida T, Sawamoto N, Araki J, Kikuchi K, et al. Pathological steps of cancer-related lymphedema: histological changes in the collecting lymphatic vessels after lymphadenectomy. *PLoS One*. 2012;7:e41126. doi: 10.1371/journal.pone.0041126
49. Gagliardi M, Ashizawa AT. The challenges and strategies of antisense oligonucleotide drug delivery. *Biomedicines*. 2021;9:433. doi: 10.3390/biomedicines9040433
50. Adachi H, Hengesbach M, Yu Y-T, Morais P. From antisense RNA to RNA modification: therapeutic potential of RNA-based technologies. *Biomedicines*. 2021;9:550. doi: 10.3390/biomedicines9050550